

In-situ Local Part Qualification of SLM 304L Stainless Steel through Voxel Based Processing of SWIR Imaging Data

Cody S. Lough¹, Xin Wang¹, Robert G. Landers¹, Douglas A. Bristow¹,
James A. Drallmeier¹, Edward C. Kinzel²

¹Department of Mechanical and Aerospace Engineering, Missouri University of Science and
Technology, Rolla, MO 65409

²Department of Aerospace and Mechanical Engineering, University of Notre Dame,
Notre Dame, IN 46556

Abstract

This paper demonstrates the potential for qualification through local part property prediction of 304L stainless steel parts manufactured by Selective Laser Melting (SLM). This is accomplished through voxel based processing of SWIR imaging data measured in-situ. Thermal features are extracted from time-series SWIR imaging data recorded from layer-to-layer to generate 3D point cloud reconstructions of parts. The voxel based data is indexed with localized measurements of SLM part properties (light-to-dark microstructural feature ratio, microhardness, μ CT data) to demonstrate the correlations. Various features are extracted from the thermal history for comparison of their respective abilities to predict the resulting local part properties. The correlations and comparisons developed in this paper are then used to discuss the capability of a voxel based framework using information from in-situ measurements of the thermal history to locally qualify parts manufactured by SLM. This work was funded by the Department of Energy's Kansas City National Security Campus which is operated and managed by Honeywell Federal Manufacturing Technologies, LLC under contract number DE-NA0002839.

1.0. Introduction

The incorporation of in-situ radiometry during Selective Laser Melting (SLM), a powder bed based Additive Manufacturing (AM) technology, provides a better understanding of the manufacturing process through non-contact measurement of emitted signals. The measurement and processing of radiometric signals provides insight into the complex thermal history experienced by a part during the manufacturing process. The complex thermal history is a result of the laser processing parameters, scan pathing, and part geometry, and can vary significantly in the volume of parts. This is an issue since the thermal history (along with material chemistry) determines the part microstructure and mechanical properties. The variances in the thermal history can lead to non-uniformity in the properties of SLM parts and defects. Measuring the variances in the thermal history allows informed decisions to be made in the production of SLM parts. The information from radiometric measurement methods can be used to identify defects, develop correlations with part properties, and make predictions of part properties resulting from SLM.

Various instrumentation including visible cameras, infrared cameras, pyrometers, and photodiodes have been used in studies to obtain information (apparent melt pool geometry, intensity/temperature, laser spatter, etc.) from the radiometric signals [1]. The features extracted from the measurements performed during the SLM process have been analyzed for various

processing conditions [2] and mapped to generate 2D and 3D data sets for parts [3]. Data processing methods have been developed for analysis of both time series data and voxel based maps of powder bed based AM parts to identify defects (melt pool quality, variances in the thermal history, porosity, failure of parts, etc.) [4-10]. Efforts are found in the literature to explore how these defects change with SLM processing conditions with an example in [11]. The understanding of this relationship has been expanded in a limited number of reports by correlating the AM part properties (tensile strength, porosity) with the information extracted from radiometric measurements [12-14].

The studies conducted to understand how radiometric signals relate to part quality and properties have shown the technique to be success. However, there is an ongoing need to mature the radiometric monitoring methods for the SLM process to enable in-situ part qualification with high confidence and simultaneous prediction of the part properties. The ability to predict bulk part properties has been explored through the development of models informed by FEA, or experimental part property measurements. In these works, the predictions of SLM part quality and properties include residual stress [15,16], porosity [17,18], mechanical performance [18], surface roughness [19], and microstructure [20]. These bulk predictions of part properties are valuable, but understanding the thermal history through experimental radiometric measurements permits the ability to predict part properties on a local basis. The radiometric measurements are necessary due to the previously discussed complex nature of the SLM process, where the variances in the local thermal history can affect the properties. The ability to make predictions of the variances in local part properties adds value to a radiometric process monitoring framework by providing a fundamental insight into how measured local processing conditions ultimately relate to the SLM part properties.

There are very few reports in the literature in the high potential area of predicting local SLM part properties through in-situ radiometric measurements. Coeck et al. demonstrated that melt pool event information measured with photodiodes can be used to detect and predict porosity in samples with high efficiency [21]. While this approach works well, recording the entire spatial and temporal components of the thermal history through thermographic imaging could provide some advantages over photodiodes with the cost of sampling frequency. Recording the spatial and temporal components of the SLM thermal history permits the effects of material re-melting to be included in predictions of part properties. Data processing of measurements from thermographic imaging can also be expanded to incorporate spatial (temperature gradients) and temporal derivatives (cooling rates), which are related to the final part microstructure.

In this paper, the ability to use thermographic imaging in the prediction of local SLM part properties (microstructure, microhardness, porosity) is explored as a part of an effort toward local part qualification. The advantage of this method to account for re-melting of material was used in this work (incorporation of derivative data will be completed in the future). To accomplish the goal of local part property predictions, a Short-Wave Infrared (SWIR) imaging camera was used to record the thermal history during SLM of 304L stainless steel. Thermal features were extracted from the time-series SWIR imaging data (time above threshold and maximum radiance) and used to develop models for predicting the local part properties. The framework was then used to predict the local part properties of an SLM part with a complex embedded feature.

2.0. Experimental Setup

2.1. Samples for Local Property Correlations and Predictions

The two samples illustrated in Fig. 1 were manufactured by using a Renishaw AM250 and 304L stainless steel powder. The AM250 is a SLM system that processes samples with a fiber laser ($P_{\max} = 200$ W, $\lambda = 1070$ nm) scanning with a point-to-point exposure strategy. The first sample was used to develop correlations between thermal features measured through SWIR imaging and local SLM part properties. This sample (Fig. 1. (a)) was partitioned into 20 sections of 20 layers for assigning various laser processing parameters. This generated a range in local thermal histories and part properties. The laser processing parameters varied in this work included the power, $P = 100 - 200$ W, and exposure time, $t_e = 50 - 125$ μ s (point distance, $d_p = 60$ μ m, and hatch spacing, $s_h = 85$ μ m, held constant). The various process parameter combinations resulted in fluence values (optical energy per unit area) ranging from 1.3 J/mm² to 6.5 J/mm². The various fluence values were randomized before assigning them to the sections of the part. Manufacturing the first sample by this procedure assumed that an increasing the distance in the build direction does not significantly impact the thermal history of parts for a constant layer-to-layer time. The procedure also assumes layer-to-layer steady state is reached for the part thermal history in the base (50 layers) and changing the parameters between the sections resulted in convergence to steady state for that parameter set immediately.

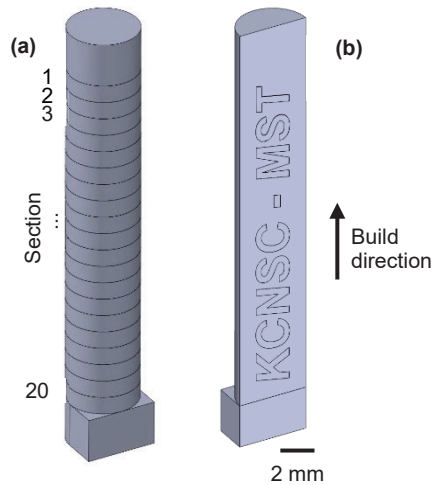


Fig. 1. CAD model of (a) various parameters sample and (b) embedded feature sample cross-section.

The correlations developed by analysis of the various parameter set sample were used with new SWIR imaging measurements from a second sample to predict its local part properties. This second SLM 304L sample (Fig. 1. (b)) was manufactured with an embedded feature of text processed with a laser power of 100 W (surrounding geometry processed with 200 W). Both the surrounding geometry and text features of this second sample were built with border scans. Processing the second sample in the described way led to the potential for local variances in part microstructure and mechanical properties due to several factors. The first factor was the lower laser power leading to sub-optimal mechanical properties and an increase in lack of fusion porosity in locations corresponding to the text interior. Additionally, at the edges of the text border scans

re-melting material could cause differences in microstructure due to changes in thermal boundary conditions during and after solidification. The border scans could have also led to an increase in porosity due to keyholing (repeated energy input in localized region). Finally, the differences in cross-sectional area processed for the text and surrounding regions led to changes in scan pathing from layer-to-layer. This introduced the potential for geometric dependence for local part properties. The predictions of the local part properties for the embedded feature sample were validated through experimental measurements.

2.2. Voxel based Processing of SWIR Imaging Data

The Renishaw AM250 used to manufacture the samples for this work contains a FLIR SC6201 SWIR imaging camera (sensitive: $\lambda = 0.9\text{-}1.7\ \mu\text{m}$, filtered: $\lambda = 1.45 \pm 0.05\ \mu\text{m}$) installed in a staring configuration to record the SLM process layer-to-layer. For this work, the camera was windowed to an 80 by 80 pixel array ($\sim 130\ \mu\text{m}/\text{pixel}$) to enable high frame rate recording ($\sim 2500\ \text{Hz}$) during SLM of the samples. Figure 2 is an illustration of the camera observing the SLM process where it collects time-series radiance data for each pixel in the image array. The measured time-series data from two locations of a layer in the various parameter set sample is plotted in Fig. 2 (b). The time series data is from the middle of the part (location 1) and the border scan region (location 2). In Fig. 2 (b), differences in the shape, number, and frequency of heating and cooling curves are observable when comparing the data from the two locations. These differences in the time-series data potentially correlate to differences in the local part properties across the part. In this work, thermal features have been extracted from the raw time-series radiance data to compress the data and allow informative correlations to be made with local part properties. Thermal feature extraction compresses the data for a layer from $\sim 100\ \text{MB}$ to $\sim 0.003\ \text{MB}$ by converting the time-series radiance data, $L(x,y,t)$, to a single feature image per layer, $f(x,y)$. This enables efficient processing and storage of SWIR imaging data measured for SLM parts.

A voxel based method was used to extract the thermal features from the time-series radiance data. The thermal features extracted in this work were the time above threshold, τ , and the maximum radiance L_{max} . The time above threshold and maximum radiance are illustrated on a section of the radiance curve from location 2 in Fig. 2 (c). The time above threshold is the total time a pixel is above the apparent phase transition region. As discussed, extraction of the thermal features from each pixel in the camera array results in a 2D map for each layer of a part. The thermal feature map (time above threshold) for the layer from the various parameters sample is illustrated in Fig. 2 (d). This figure shows the variances in the thermal feature across this layer of the part where higher thermal feature values are measured at the edges of parts due to the laser cornering and border scans. After performing feature extraction for each layer in a part, the data can be arranged to generate voxel reconstructions based on the thermal history. This is illustrated for the various process parameters sample in Fig. 2 (d). The voxel reconstructions of parts can be sliced for inspection and processed further to identify differences and make predictions of local part properties.

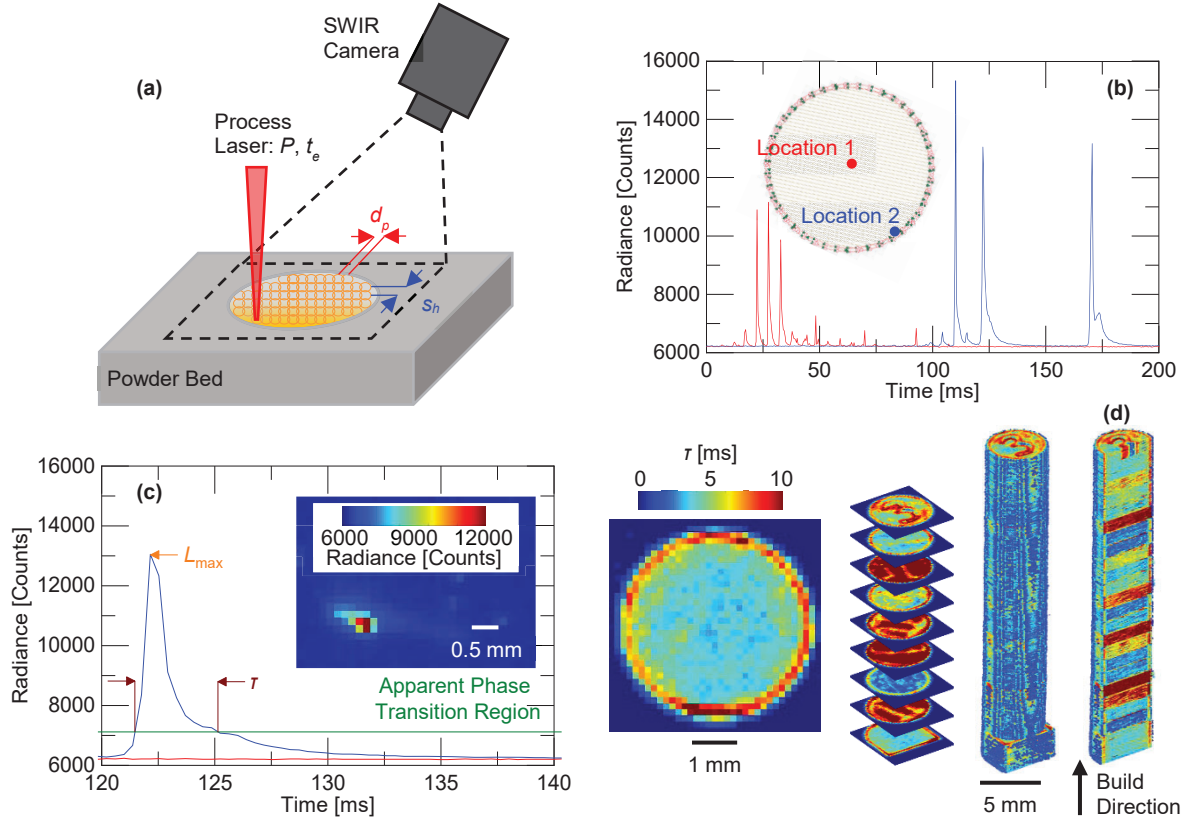


Fig. 2. (a) SWIR camera observation of SLM process, (b) time series data from location in center of part cross-section (location 1) and border scan region (location 2), (c) definition of thermal features in time series data with melt pool image, and (d) thermal feature maps showing generation of volumetric data and slicing.

2.3. Local Part Property Measurements

The local part properties measured in this work included the light-to-dark microstructural feature ratio, $LDFR$, the microhardness, HV , and the volumetric porosity, ϕ . Fig. 3 (a) demonstrates the light and dark microstructural features in the etch response of SLM 304L stainless steel (polished to $0.05 \mu\text{m}$, electrolytically etched with 40/60 nitric acid). The light and dark features are due to differences in the solidification mode, which is described in [22]. The light feature corresponds to material that solidified as ferrite and then transformed into austenite upon further cooling. The dark feature corresponds to material that solidified as austenite and remained austenite. Mapping the ratio of these features within the part cross-sections provided insight into the solidification mode that was most prominent for a particular region. This was completed through implementation of an image processing framework developed in MATLAB. The Vicker's microhardness (representative indent in Fig. 3 (b), 4.9 N and 10 seconds) was mapped in the part cross-sections following ASTM E384-17 [23]. The porosity in the volume of samples was determined through processing micro-computed tomography (micro-CT) data. This was accomplished by assuming voxels with intensity values three standard deviations less than the mean intensity value of a solid volume corresponded to porosity. The micro-CT data for the parts was down-sampled to the resolution of the SWIR imaging data by determining the percentage of

porosity voxels in a 130 μm by 130 μm by 50 μm volume. This process is illustrated for a slice of the various parameter set sample micro-CT data in Fig. 3 (c).

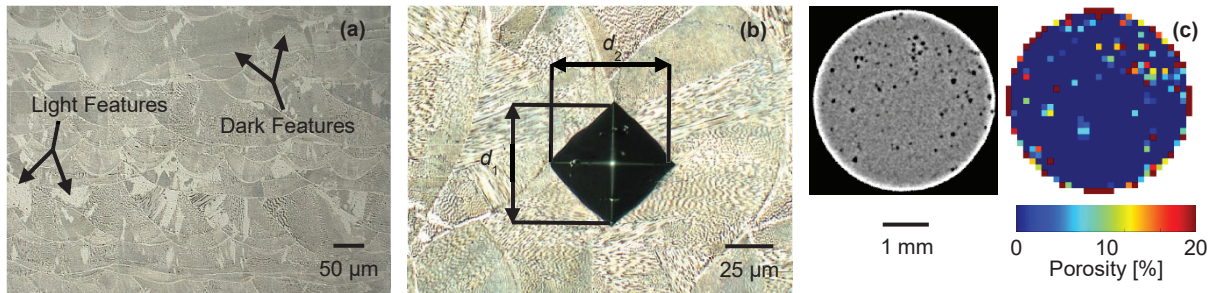


Fig. 3. (a) Optical micrograph of 304L stainless steel showing light and dark microstructural features, (b) micrograph of indent for determining microhardness, and (c) micro-CT slice with processing to determine voxel based local porosity.

3.0. Local Part Properties Correlations

The following details the development of the correlations between local part properties and thermal feature measurements using data from the various parameter set sample. The *LDFR* and microhardness were determined for the cross-section of the part, while the porosity was measured for the entire volume. Figure 4 contains the data maps for the cross-section of the sample. Figure 4 (a) is the etched micrograph of the sample that shows differences in the amount of porosity and etch response for the different fluence inputs (values annotated to the left). The *LDFR* plotted in Fig. 4 (b) shows that higher fluence values corresponds to more of the light feature within a section. The increase in the light feature is due in part to differences in thermal boundary conditions during and after solidification. The increase in light feature is also because more energy input leads to larger melt pools and more overlap of laser scans. This leads to more re-melting within the parts which corresponds to an increase in the light feature. The same effect is observed for the border scan regions of parts. The microhardness for the part mapped in Fig. 4 (c) appears qualitatively uniform except in areas corresponding to low fluence values where the part was softer, or a pore led to no measurement. The porosity from micro-CT scanning of the part is displayed in Fig. 4 (d) and shows that low fluence values resulted in an increase in porosity. The time above threshold and maximum radiance thermal feature reconstructions are included as Fig. 4 (e) and Fig. 4 (f), respectively. Qualitative comparisons of the thermal features and local part properties shows that low feature values correspond to low *LDFRs*, low microhardness, and high porosity. High thermal feature values generally correspond to higher *LDFRs*, uniform microhardness, and low amounts of porosity.

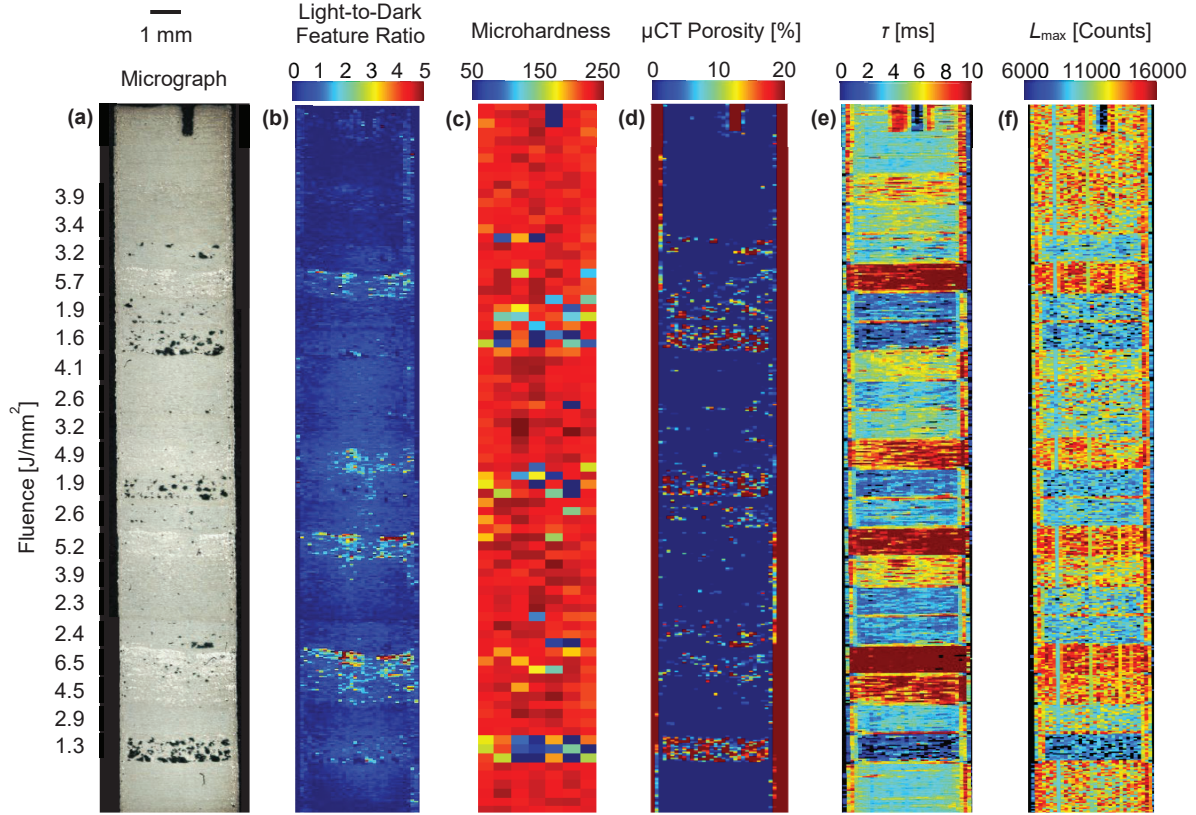


Fig. 4. (a) Optical micrograph after etching, (b) *LDFR*, (c) microhardness, (d) porosity, (e) time above threshold, and (f) maximum radiance in cross-section of various process parameters sample.

Figure 4 shows qualitatively clear relationships between local part properties and thermal features. The local part property values and thermal features have been averaged for the various sections of the sample for correlation development through data-driven modeling. The correlations between the *LDFR* and thermal features are plotted in Fig. 5. Each data point for the *LDFR* is the average and standard deviation from ~ 600 pixels. The corresponding thermal feature values are the averages and standard deviations from ~ 7000 voxels. The *LDFR* as a function of thermal features was fit to a second order polynomial. The thermal feature of time above threshold demonstrated a slightly stronger relationship with the *LDFR* than the maximum radiance.

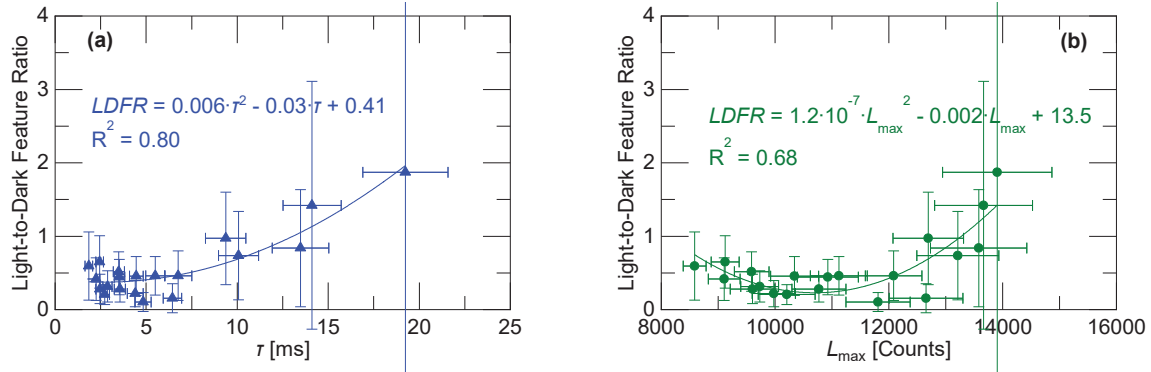


Fig. 5. Correlation of average *LDFR* with (a) average time above threshold and (b) average maximum radiance.

Figure 6 is the correlation of the averaged microhardness from the various energy inputs with the corresponding thermal feature measurements. Each microhardness value is the average and standard deviation from 20 measurements. Thermal feature values are again from ~ 7000 voxels. In this figure, the saturation of microhardness is apparent with the additional detail of a slightly decreased microhardness for some of the higher thermal feature values. The relationship between microhardness and the thermal features were fit to a lumped capacitance model. The feature of time above threshold demonstrated a stronger relationship with the microhardness.

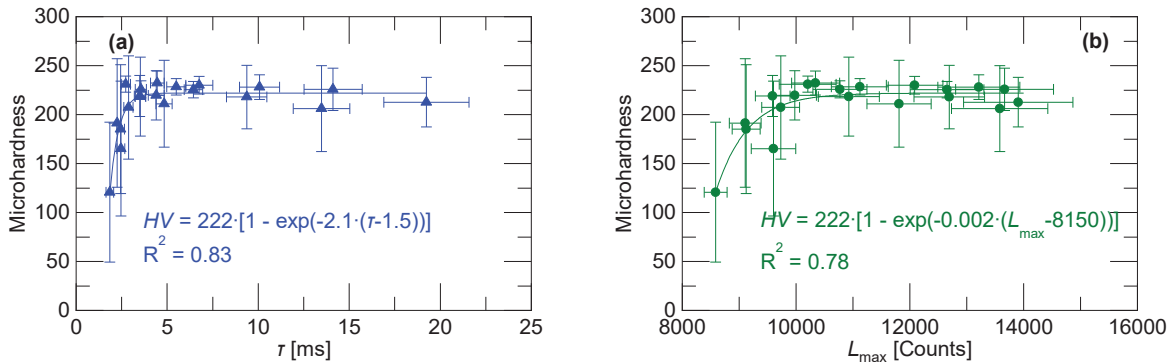


Fig. 6. Correlation of average microhardness with (a) average time above threshold and (b) average maximum radiance.

Figure 7 contains the fits of porosity determined by micro-CT as a function of the thermal features. Both the micro-CT porosity values and the thermal feature values are the averages and standard deviations over volumes of the part corresponding to ~ 7000 voxels. In Fig. 7, two regions of porosity greater than 1% are observable. The first high porosity region corresponds to lower thermal values and is a result of lack of fusion. The second region corresponds to higher thermal feature values and is due to keyholing. The piecewise nature of the porosity-thermal feature relationship led to fitting a linear model for each porosity regime.

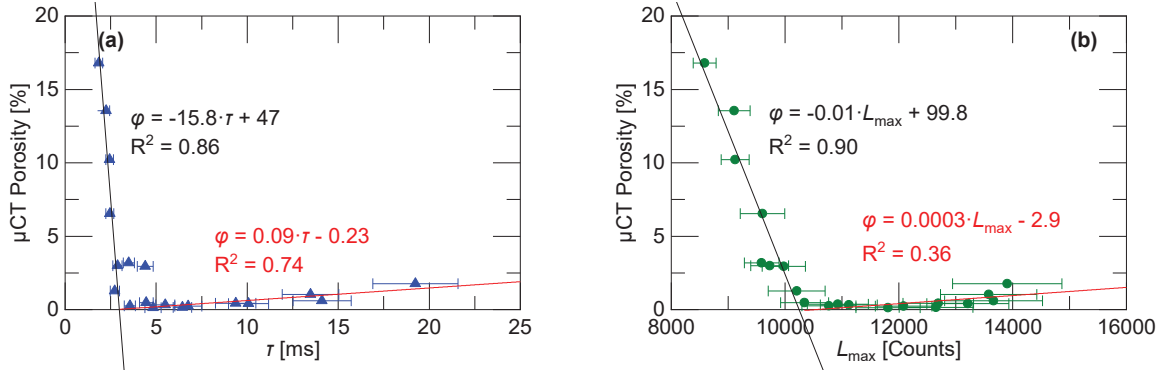


Fig. 7. Correlation of porosity determined from micro-CT data with (a) average time above threshold and (b) average maximum radiance.

4.0. Prediction of Local Part Properties

Modeling the relationships between thermal features and the local part properties permits predictions for new parts through SWIR imaging measurements. This is demonstrated in Fig. 8 where the models developed in the previous section are applied to the time above threshold thermal feature measurement for the embedded text sample. In this figure, local part property predictions are made for the entire volume of the part. The measured thermal feature predicts significant variation in the local part properties for the sample in the locations corresponding to the embedded text. The local part property predictions for the embedded feature sample were made by using both the time above threshold and maximum radiance.

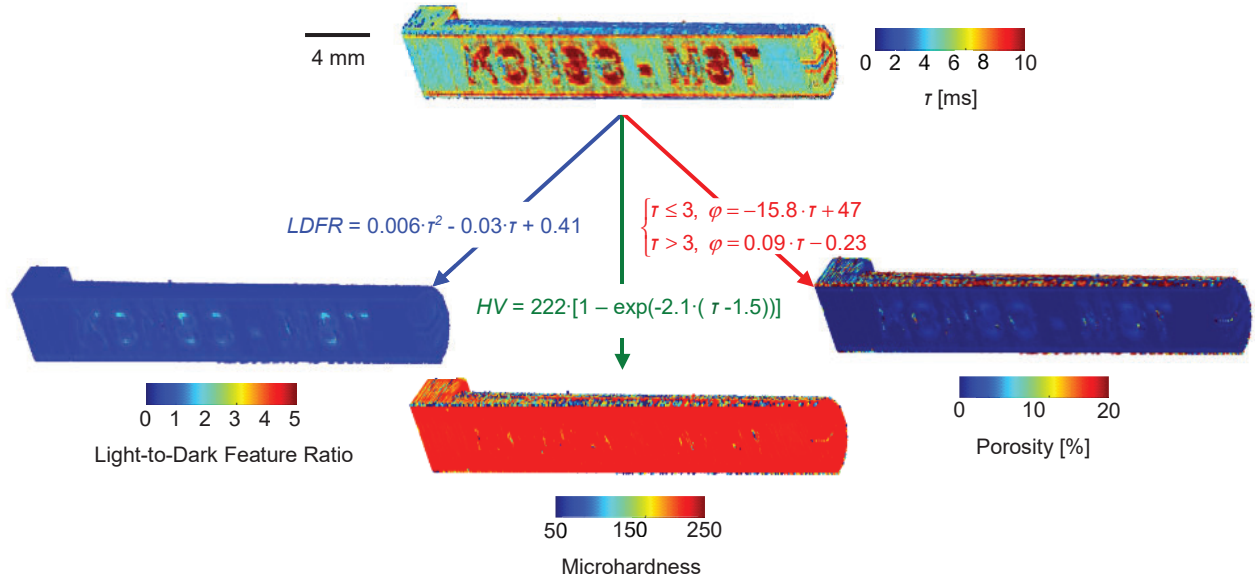


Fig. 8. Demonstration of local part properties predictions using models developed in correlations with thermal feature measurements.

Figure 9 contains the time above threshold prediction of the local part properties plotted next to the experimental measurements. These results are for the cross-section of the embedded feature sample (micrograph included for reference). Figure 9 shows that the predicted areas of

increased *LDFR* corresponding to the text border areas match the results found in experimental measurements. The time above threshold was also able to predict the decrease in microhardness for areas corresponding to the text interior. The porosity predictions from the time above threshold show localized areas of high amounts of porosity for the text interiors. There is also the prediction of a slight increase in porosity at the location of the text borders. These results are similar to the experimental porosity measurements.

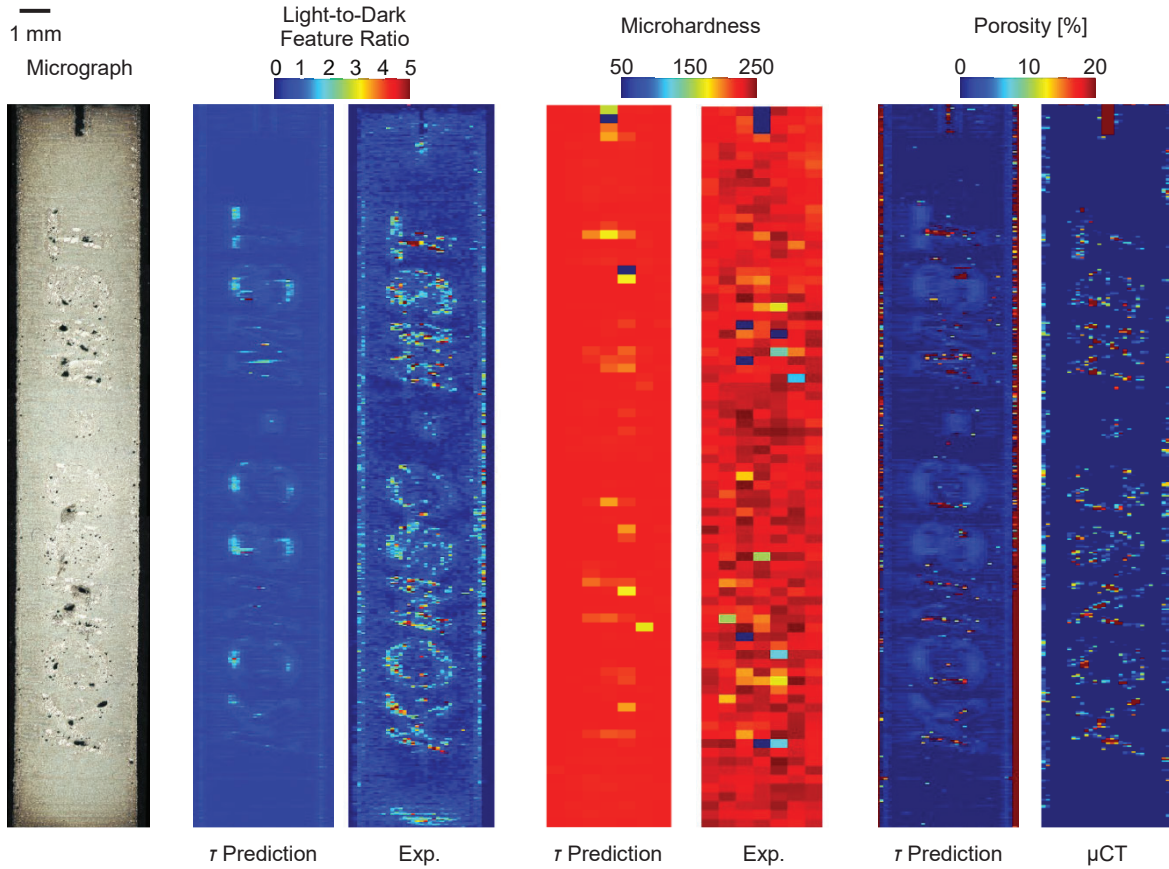


Fig. 9. (a) Etched micrograph of embedded feature specimen cross-section and comparison of time above threshold predictions with experimental maps of (b) *LDFR*, (c) microhardness, and (d) porosity.

Figure 10 contains a comparison of the maximum radiance predictions with the experimental local part property measurements of the embedded feature sample. In this figure, the *LDFR* and porosity predictions have increased noise. There are also a larger number of predicted locations around the text that are softer in the maximum radiance predictions.

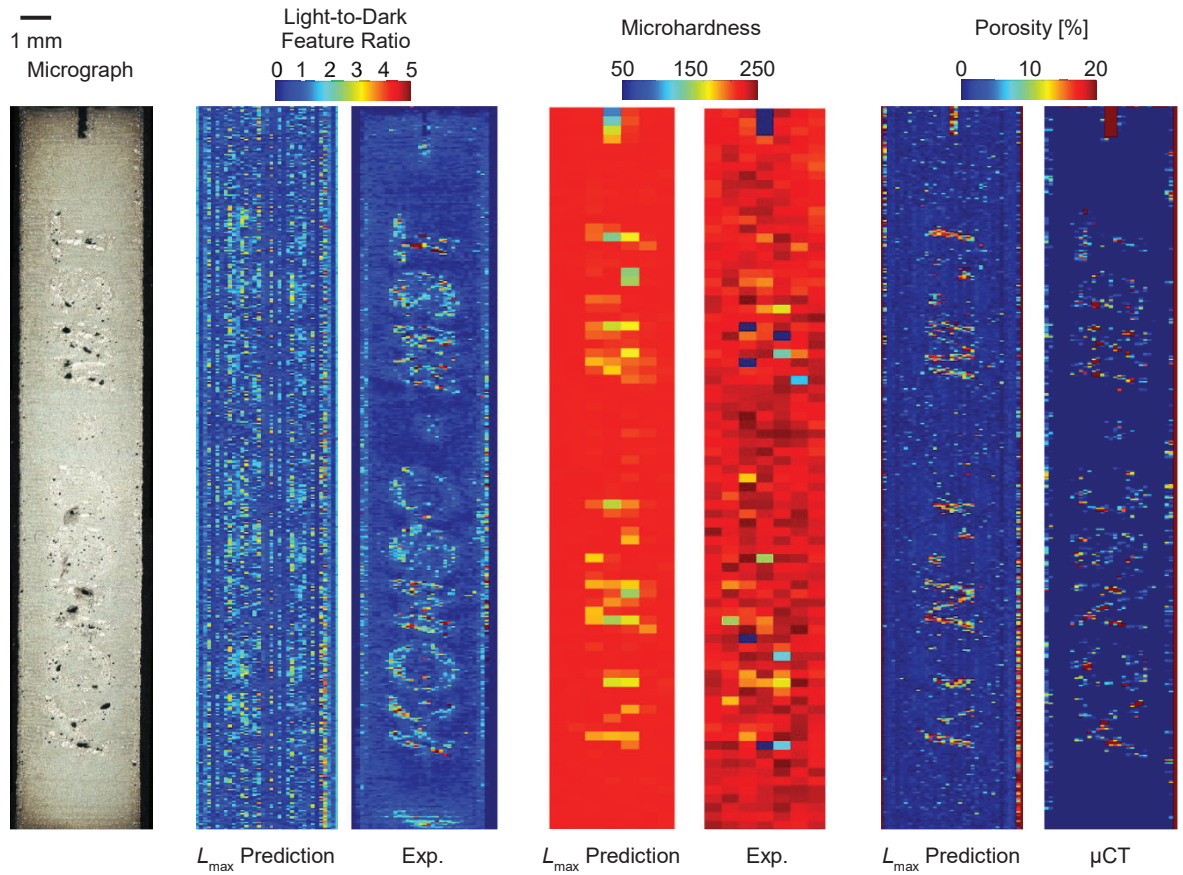


Fig. 10. (a) Etched micrograph of embedded feature specimen cross-section and comparison of maximum radiance predictions with experimental maps of (b) *LDFR*, (c) microhardness, and (d) porosity.

The error of this method has been quantified by subtracting the experimental results from the thermal feature predictions. The error maps for both the time above threshold and maximum radiance predictions are plotted with the experimental local part property maps in Fig. 11. These maps show that the thermal features predict the properties of the part with some error. There is an increase in error around the embedded text, but the increase is tolerable. To demonstrate this, histograms of the error were generated for the cross-sections of *LDFR* and microhardness predictions and for the volumes of the porosity predictions.

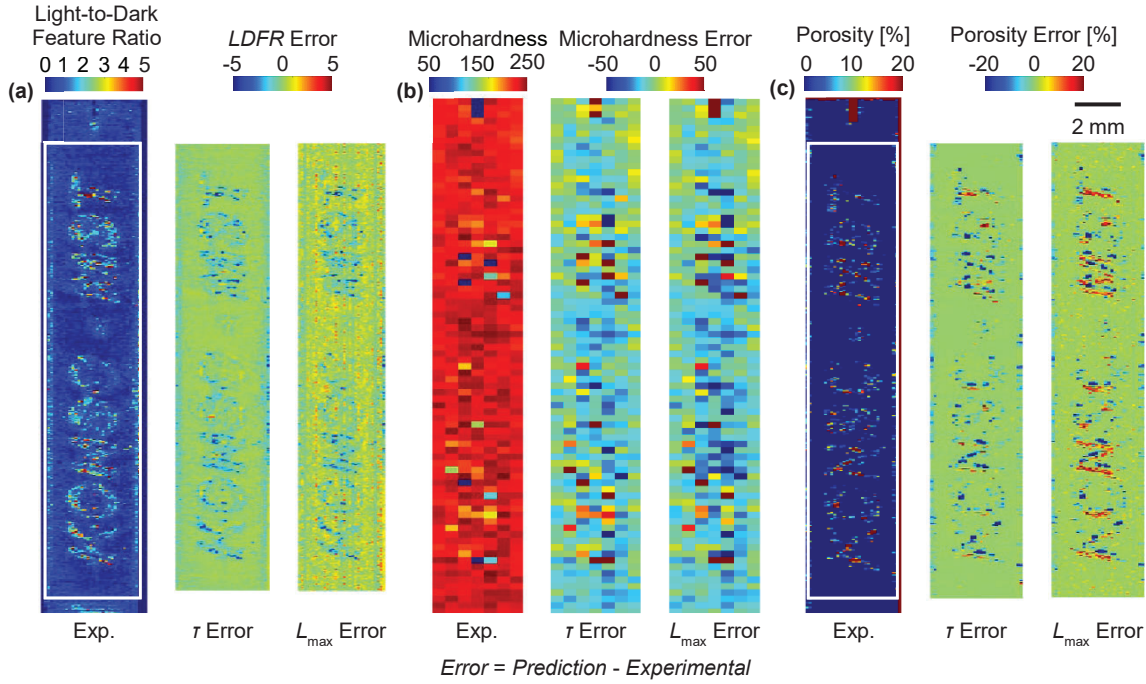


Fig. 11. Experimental and prediction error maps for (a) *LDFR*, (b) microhardness, and (c) porosity.

Figure 12 contains the error distribution for the thermal feature predictions of the local part properties (outliers excluded in plots). Figure 12 (a) shows that a majority of the errors for the *LDFR* predictions fell between values of -2 and 4 (error over $\sim 13,000$ pixels). The time above threshold performed slightly better in predicting the *LDFR* when compared to the maximum radiance. In Fig. 12 (b), similar errors for the predictions are seen and most of the error was found between hardness values of -40 and 30 (error over ~ 570 pixels). The error for microhardness is offset from 0 due to the models developed in Fig. 6. In the models from Fig. 6, the microhardness saturates at a value of ~ 222 and this is ~ 7 hardness values less than the mean for the surrounding of the embedded feature sample. Figure 12 (c) shows that a majority of porosity error was between 0 and 2% for both thermal feature predictions (error over $\sim 580,000$ voxels). The time above threshold also performed better for this local part property. It should be noted that a reduction in the reported error is possible by improving the indexing of predictions and experimental methods and with the development of stronger models for the relationships between thermal features and local part properties.

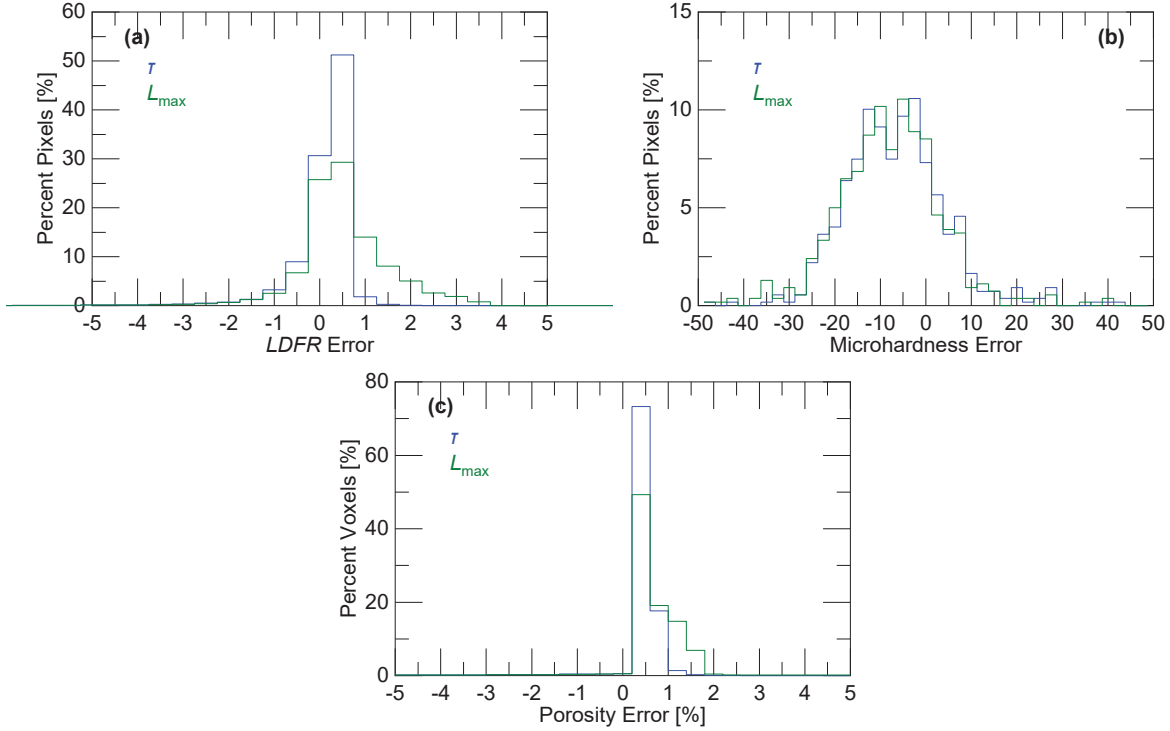


Fig. 12. Error distribution for thermal feature predictions of (a) *LDFR*, (b) microhardness, and (c) porosity.

In Figs. 9 and 10, both the time above threshold and maximum radiance were able to qualitatively predict the variances in the local part properties in the embedded feature sample. Quantifying the error of the predictions in Figs. 11 and 12 showed that the time above threshold performed the best for the *LDFR* and porosity. This is because the time above threshold accounts for the total amount of time the radiance of a voxel is above the apparent phase transition region. This is a strong thermal feature to use in predicting the *LDFR* since the microstructural feature is related to the total number of times the material is re-melted. The time above threshold feature is also better for porosity predictions because the more time a voxel is above the apparent phase transition region the more likely it is to correspond to fully dense material. Additionally, the increase in porosity due to keyholing was related more strongly to the time above threshold which led to better predictions. In general, the increased error of maximum radiance predictions is due to weaker correlations with the local part properties and a larger amount of noise in the measurement. The errors of the microhardness predictions were within the standard deviations of the experimental measurements corresponding to the extreme energy inputs in Fig. 6 for both thermal features. The results in Figs. 8-12 show that predictions of local SLM part properties can be made with tolerable error for complex features in SLM parts.

5.0. Summary and Conclusions

In this paper, a voxel based framework was used to process SWIR imaging data measured in-situ and make predictions of SLM 304L stainless steel part properties on a local basis. Thermal features including the time above threshold and maximum radiance were extracted from time-series SWIR imaging data and correlated with the local part properties. The time above threshold

was found to correlate the strongest when developing models of the local part properties as a function of the thermal features. The developed models were used to make predictions of the local part properties based on new thermal feature measurements for an SLM sample manufactured with an embedded feature and the error was quantified. The time above threshold outperformed the maximum radiance in making predictions of the *LDFR* and porosity, but performed similarly for microhardness.

The errors of the local part property predictions could be reduced by moving towards machine learning algorithms with the incorporation of multiple thermal features that capture different dynamics of the SLM process. The framework reported in this paper can be used to qualify parts, or flag them for further ex-situ analysis, on a local basis with further development. In this further development, confidence intervals for the minimum size of defective local part property variation predictable will be defined.

Acknowledgment

This work was funded by Honeywell Federal Manufacturing & Technologies under Contract No. DE-NA0002839 with the U.S. Department of Energy. The United States Government retains and the publisher, by accepting the article for publication, acknowledges that the United States Government retains a nonexclusive, paid up, irrevocable, world-wide license to publish or reproduce the published form of this manuscript, or allow others to do so, for the United States Government purposes.

References

- [1] M. Grasso and B.M. Colosimo, Process defects and in situ monitoring methods in metal powder bed fusion: a review, *Measurement Science and Technology* 28 (2017) 1-25.
- [2] Y. Zhang, J.Y.H. Fuh, D. Ye, G.S. Hong, In-situ monitoring of laser-based PBF via off-axis vision and image processing approaches, *Additive Manufacturing* 15 (2019) 263-274.
- [3] H. Krauss, T. Zeugner, M.F. Zaeh, Layerwise monitoring of the selective laser melting process by thermography, *Physics Procedia* 56 (2014) 64–71.
- [4] T. Craeghs, S. Clijsters, J.-P. Kruth, F. Bechmann, M.-C. Ebert, Detection of process failures in layerwise laser melting with optical process monitoring, *Physics Procedia* 39 (2012) 753–759.
- [5] J. Mireles, S. Ridwan, P.A. Morton, A. Hinojos, R.B. Wicker, Analysis and correction of defects within parts fabricated using powder bed fusion technology, *Surface Topography: Metrology and Properties* 3 (2015) 1–8.
- [6] J.L. Bartlett, F.M. Heim Y.V. Murty, X. Li, In situ defect detection in selective laser melting via full-field infrared thermography, *Additive Manufacturing* 24 (2018) 595-605.
- [7] L. Scime, J. Beuth, Anomaly detection and classification in a laser powder bed additive manufacturing process using a trained computer vision algorithm, *Additive Manufacturing* 19 (2018) 114-126.
- [8] S. Yoder, P. Nandwana, V. Paquit, M. Kirka, A. Scopel, R.R. Dehoff, S.S. Babu, Approach to qualification using E-PBF in-situ process monitoring in Ti-6Al-4V, *Additive Manufacturing* 28 (2019) 98-106.
- [9] B.M. Colosimo, M. Grasso, Spatially weighted PCA for monitoring video image data with application to additive manufacturing, *Journal of Quality Technology* 50 (4) (2018) 391-417.

- [10] L. Scime, J. Beuth, Using machine learning to identify in-situ melt pool signatures indicative of flaw formation in a laser powder bed fusion additive manufacturing process, *Additive Manufacturing* 25 (2019) 151-165.
- [11] G. Kasperovich, J. Haubrich, J. Gussone, G. Requena, Correlation between porosity and processing parameters in TiAl6V4 produced by selective laser melting
- [12] M. Bisht, N. Ray, F. Verbist, S. Coeck, Correlation of selective laser melting-melt pool events with the tensile properties of Ti-6Al-4V ELI processed by laser powder bed fusion, *Additive Manufacturing* 22 (2018) 302-306.
- [13] P. Nandwana, M.M. Kirka, V.C. Paquit, S. Yoder, R.R Dehoff, Correlations between powder feedstock quality, in situ porosity detection, and fatigue behavior of Ti-6Al-4V fabricated by powder bed electron beam melting: a step towards qualification, *JOM* 70 (9) (2018) 1686-1691.
- [14] Q.Y. Lu, N.V. Nguyen, A.J.W. Hum, T. Tran, C.H. Wong, Optical in-situ monitoring and correlation of density and mechanical properties of stainless steel parts produced by selective laser melting process based on varied energy density, *Journal of Materials Processing Technology* 271 (2019) 520-531.
- [15] C. Li, C.H. Fu, Y.B. Guo, F.Z. Fang, A multiscale modeling approach for fast prediction of part distortion in selective laser melting, *Journal of Materials Processing Technology* 229 (2016) 703-712.
- [16] H.S. Park, N.H. Tran, D.S. Nguyen, Development of a predictive system for SLM product quality, *IOP Conference Series: Materials Science and Engineering* 227 (2017) 012090.
- [17] G. Tapia, A.H. Elwany, H. Sang, Prediction of porosity in metal-based additive manufacturing using spatial Gaussian process models, *Additive Manufacturing* 12 (2016) 282-290.
- [18] G. Miranda, S. Faria, F. Bartolomeu, E. Pinto, S. Madeira, A. Mateus, P. Carreira, N. Alves, F.S. Silva, O. Carvalho, Predictive models for physical and mechanical properties of 316L stainless steel produced by selective laser melting, *Materials Science & Engineering A* 657 (2016) 43-56.
- [19] G. Strano, L. Hao, R.M. Everson, K.E. Evans, Surface roughness analysis, modeling, and prediction in selective laser melting, *Journal of Materials Processing Technology* 213 (2013) 589-597.
- [20] J. Liu, A.C To, Quantitative texture prediction of epitaxial columnar grains in additive manufacturing using selective laser melting, *Additive Manufacturing* 16 (2017) 58-64.
- [21] S. Coeck, M. Bisht, J. Plas, F. Verbist, Prediction of lack of fusion porosity in selective laser melting based on melt pool monitoring data, *Additive Manufacturing* 25 (2019) 347-356.
- [22] J.C. Lippold, Solidification behavior and cracking susceptibility of pulsed-laser welds in austenitic stainless steels, *Welding Research Supplement* (1994) 129-139.
- [23] ASTM E384 Standard test method for microindentation hardness of materials, ASTM International, West Conshohocken, PA, (2017).